Available online at www.sciencedirect.com
ScienceDirect
Trans. Nonferrous Met. Soc. China 30(2020) 1717−1730
Transactions of Nonferrous Metals Society of China
www.tnmsc.cn

Effect of thermal exposure on microstructure and mechanical properties of Al−Si−Cu−Ni−Mg alloy produced by different casting technologies

Jia-ying ZHANG[†1], Li-jie ZUO[†2], Jian FENG[3], Bing YE[1], Xiang-yang KONG[4], Hai-yan JIANG[1], Wen-jiang DING[1]

1. National Engineering Research Center of Light Alloy Net Forming and State Key Laboratory of Metal Matrix Composites, Shanghai Jiao Tong University, Shanghai 200240, China;
2. School of Mechanical and Ocean Engineering, Jiangsu Ocean University, Lianyungang 222005, China;
3. GRIMAT Engineering Institute Co., Ltd., Beijing 101407, China;
4. Institute of Materials for Mobile Energy, School of Materials Science and Engineering, Shanghai Jiao Tong University, Shanghai 200240, China

Received 21 October 2019; accepted 2 June 2020

Abstract: The effect of thermal exposure at 350 °C for 200 h on microstructure and mechanical properties was investigated for Al−Si−Cu−Ni−Mg alloy, which was produced by permanent mold casting (PMC) and high pressure die casting (HPDC). The SEM and IPP software were used to characterize the morphology of Si phase in the studied alloys. The results show that the thermal exposure provokes spheroidization and coarsening of eutectic Si particles. The ultimate tensile strength of the HPDC alloy after thermal exposure is higher than that of the PMC alloy at room temperature. However, the TEPMC and TEHPDC alloys have similar tensile strength around 67 MPa at 350 °C. Due to the coarsening of eutectic Si, the TEPMC alloy exhibits better creep resistance than the TEHPDC alloy under studied creep conditions. Therefore, the alloys with small size of eutectic Si are not suitably used at 350 °C.
Key words: Al−Si−Cu−Ni−Mg alloy; thermal exposure; coarsening; creep behavior

1 Introduction

To develop fuel-efficient diesel engines, light-weight and high-performance piston is one of strategies pursued [1,2]. Aluminum and its alloys, hypereutectic and eutectic Al−Si alloys in particular, are widely used in the automotive industry owing to their good castability, high specific strength, low coefficient of thermal expansion (CTE), and excellent wear resistance [3−5]. However, with greater demands for engine power output, the alloys used for fabricating the piston must be served at the higher temperatures and stresses, and thus the development of superior piston alloys becomes urgent.

The aluminides such as Q-$Al_5Cu_2Mg_8Si_6$, AlSiMn(Cr)Fe, δ-Al_3CuNi and γ-Al_7Cu_4Ni are generated in Al−Si alloys with the addition of Cu, Ni, Mg, Mn and Cr elements, which significantly improved the mechanical performance of the alloys at elevated temperatures [6,7]. Some researchers attempted to adjust the content of alloy elements to develop a new alloy with higher mechanical properties [8−10]. LI et al [11] reported the effect of Cr addition on the microstructure and mechanical properties of Al−12Si−3.5Cu−2Mn heat resistant alloys. ZUO et al [10] found that the mechanical properties of Al−Si−Cu−Mg alloys increased with Cu and Mg elements. Microstructure refinement of

† Jia-ying ZHANG and Li-jie LUO contributed equally to this work.
Foundation item: Projects (2016YFB0700502, 2016YFB0301001) supported by the National Key Research and Development Program of China
Corresponding author: Bing YE; Tel: +86-21-54742715; Fax: +86-21-34202794; E-mail: bingye@sjtu.edu.cn
DOI: 10.1016/S1003-6326(20)65333-X

Al−Si−Cu−Ni−Mg heat-resistant alloy has become another research hotspot [12−14]. The transition elements such as Zr, Ti, and Sc were widely used to refine the microstructure. HAN et al [15] found that the microstructure and mechanical properties of Al−12Si−4Cu−2Ni−0.8Mg alloys varied with the Nd content. PRAMOD et al [16] reported the effect of Sc addition on the secondary dendritic arm spacing, eutectic Si modification, and intermetallic phase modification. Meantime, rapid cooling is also used to refine the microstructure of Al−Si−Cu−Ni−Mg alloy. ZHANG et al [17] reported that the ductility and ultimate tensile strength of cast A356 alloy were significantly improved with near-rapid solidification and thermo-mechanical treatment. Rapid cooling can be routinely achieved in industrial practice through high pressure die casting (HPDC). Al−Si−Cu−Ni−Mg alloy fabricated by HPDC exhibited higher mechanical properties including tensile and creep performance at elevated temperatures compared with conventional permanent mold casting (PMC) [18].

It is well known that the top of piston operates at temperature above 350 °C and peak stress above 20 MPa. The mechanical properties of the materials used to fabricate piston have to be stable under in-service condition. Therefore, it is critical and mandatory to evaluate the stability of microstructure and mechanical properties at elevated temperatures for safety-critical applications. Some researchers reported that Si with long-range three-dimensional (3-D) interconnected rigid network was considered to be the key factor for enhancing mechanical properties through load transfer mechanism [19−22]. The shape, size, distribution and connectivity of Si phase are critical for the heat-resistant Al−Si−Cu−Ni−Mg alloys. However, the evolution of Si particles was rarely studied during thermal exposure at elevated temperatures, especially for the microstructure of refined Al−Si−Cu−Ni−Mg alloys.

In this study, the evolution of Si particles in HPDC and PMC alloys was quantitatively characterized before and after thermal exposure at 350 °C for 200 h. In order to find out the relationship between changes of Si particles and mechanical properties, the tensile performances at room and elevated temperatures of the studied alloys were investigated. Furthermore, the compressive creep was also compared before and after thermal exposure to identify whether the HPDC alloy was suitable for use after thermal exposure. The results provide indispensable information for the development and designing of the piston alloys.

2 Experimental

The Al−12Si−3.5Cu−2Ni−0.8Mg alloy containing 12.0 Si, 3.5 Cu, 2.0 Ni, 0.8 Mg, 0.4 Fe, 0.15Zr, and 0.15 Ti (in wt.%), was prepared by melting high-purity Al, Mg, and Al−23%Si, Al−50%Cu, Al−10%Ni, Al−20%Fe, Al−4%Zr and Al−5%Ti commercial master alloys in a steel crucible at approximately 740 °C. After the process of refining, the melt was subsequently settled and homogenized in furnace at the temperature of 720 °C for about 10 min before casting. Finally, the melt was cast through PMC and HPDC to obtain bulk PMC and HPDC samples, respectively. Figure 1 shows the diagrams of the molds and the selected areas of PMC and HPDC alloys. The

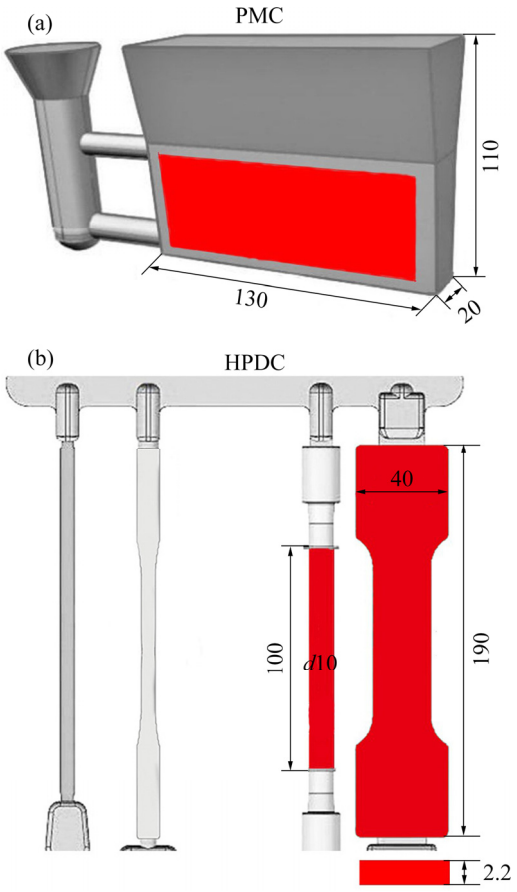

Fig. 1 Selected sections (marked with red) for preparing standard testing samples from PMC (a) and HPDC (b) alloys (unit: mm)

HPDC samples were prepared using a cold-chamber die-cast machine (TOYO BD−350 V5). The HPDC die includes a rod creep specimen with a gauge length of 100 mm and a cross section diameter of 10 mm, and a flat tensile specimen with 2.2 mm in thickness, 40 mm in width, and 190 mm in length. The detailed procedures of sample preparation including melting and casting were described in previous work [18]. In the following thermal exposure experiments, the as-cast samples were exposed at 350 °C for 200 h, followed by water quenching at 60 °C to room temperature. The PMC and HPDC samples after thermal exposure were named as TEPMC and TEHPDC, respectively.

Metallographic samples were prepared by the standard technique and then etched with Keller reagent (95 vol.% H_2O, 2.5 vol.% HNO_3, 1.5 vol.% HCl and 1 vol.% HF) for 15 s. The microstructure of each alloy was characterized by Zeiss-Axio Observer A1 optical microscopy and FEI NOVA Nano 230 field-emission scanning electron microscope (SEM) equipped with AZtec X-Max 80 X-ray energy dispersive spectroscopy (EDS).

The size, aspect ratio and roundness of eutectic Si were statistically analyzed using the image analysis software Image-Pro Plus 6.0 (IPP). The aspect ratio of eutectic Si was calculated based on the ratio of the average length to width. The roundness (R_a) of eutectic Si particles was calculated as follows [23]:

$$R_a = p^2 / (4\pi A) \quad (1)$$

where p is the perimeter and A is the area of each Si particle. To get reliable statistical character, at least 600 eutectic Si particles were analyzed for each alloy.

The flat tensile specimen with 15 mm in gauge length, 3.5 mm in width, and 2 mm in thickness was tested on a WDW−10S universal tensile tester (TE, Jinan, China) within an attached high temperature furnace controlled within ±2 °C. The tensile tests were carried out at 25 °C and 350 °C in air with a crosshead speed of 0.45 mm/min. In all elevated temperature testing, specimens were heated to the desired temperature and held for 15 min before conducting tensile tests. To ascertain reproducibility, each tensile property reported was the average value obtained from at least three tensile specimens.

Cylindrical specimens for compression creep tests with 10 mm in diameter and 10 mm in height, were cut from the TEPMC and TEHPDC alloys by an electric discharge machine (EDM). The compression creep tests were carried out inside furnace at temperatures ranging from 200 to 300 °C and applied stresses ranging from 20 to 130 MPa on an ATS 16001 creep testing machine (Butler, PA, USA). The displacement was measured by averaging from two linear variable differential transformers (LVDT) attached to the creep specimen through rigid rods.

3 Results and discussion

3.1 Microstructural evolution

Figure 2 shows the representative optical micrographs of the studied alloys. The microstructure of Al−12Si−3.5Cu−2Ni−0.8Mg PMC alloy consists of ductile α(Al) dendrites surrounded by eutectic Si and aluminides in the interdendritic region. There is no significant difference between the microstructures of the PMC and the TEPMC alloys, except for the fragmented and spheroidal eutectic Si particles (Figs. 2(a) and (c)). On the contrary, the microstructure of the HPDC alloy dramatically changes after thermal exposure as shown in Figs. 2(b) and (d). The HPDC alloy exhibits equiaxed α(Al) grain and fine eutectic Si, while TEHPDC alloy shows remarkably coarse eutectic Si with uniform distribution, and coarse α(Al) by merging equiaxed α(Al) grain and eutectic Al grain. It is hard to discriminate α(Al) grain and Al−Si eutectic. The aluminides in HPDC and TEHPDC alloys are difficult to distinguish under the optical microscopy.

The SEM images in BSE mode of the investigated alloys are shown in Fig. 3. Based on the EDS analysis, main phases of the PMC and HPDC alloys include Si, ε-Al_3Ni, δ-Al_3CuNi, and Q-$Al_5Cu_2Mg_8Si_6$ phases, as shown in Figs. 3(a) and (b), identified in previous studies [18]. No obvious differences are found for phase compositions of the two alloys after thermal exposure by comparing Figs. 3(a) and (c), and Figs. 3(b) and (d), respectively. The shapes and sizes of blocky-shape δ-Al_3CuNi and ε-Al_3Ni phases are almost constant before and after thermal exposure, indicating that these Ni-rich phases are thermally stable at 350 °C, which is in good agreement with the previous studies [7,8]. The corresponding XRD analysis after thermal exposure is shown in Fig. 4, which is consistent with phases determined by EDS.

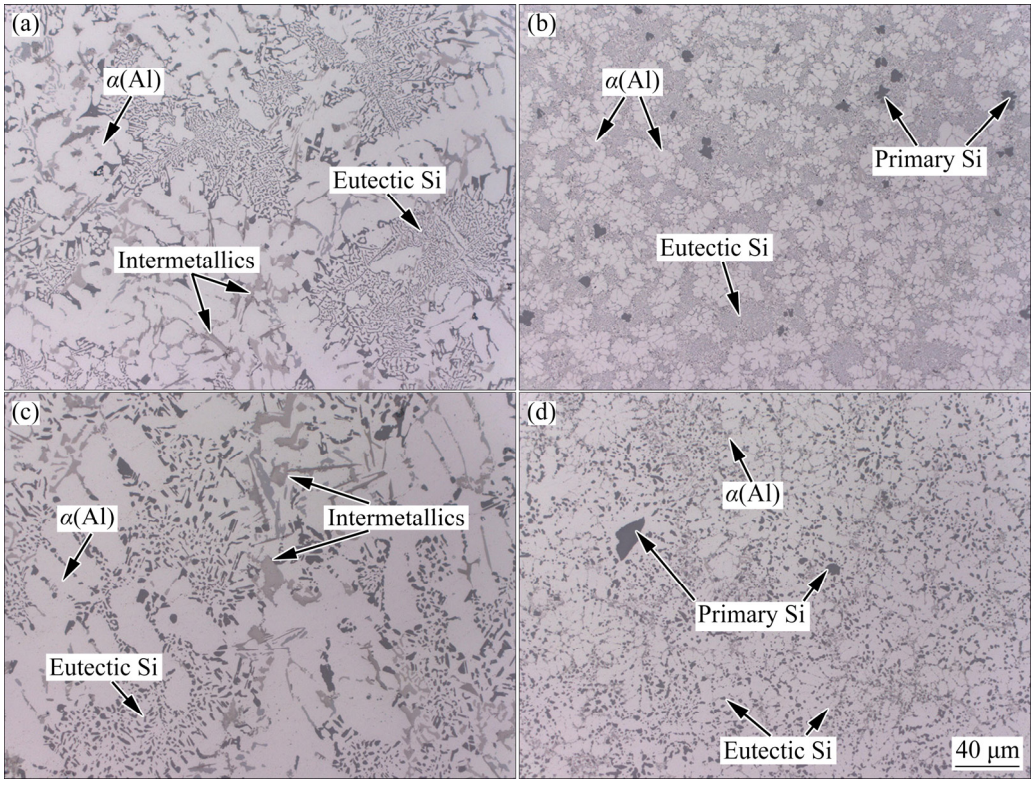

Fig. 2 Optical images of studied alloys: (a) PMC; (b) HPDC; (c) TEPMC; (d) TEHPDC

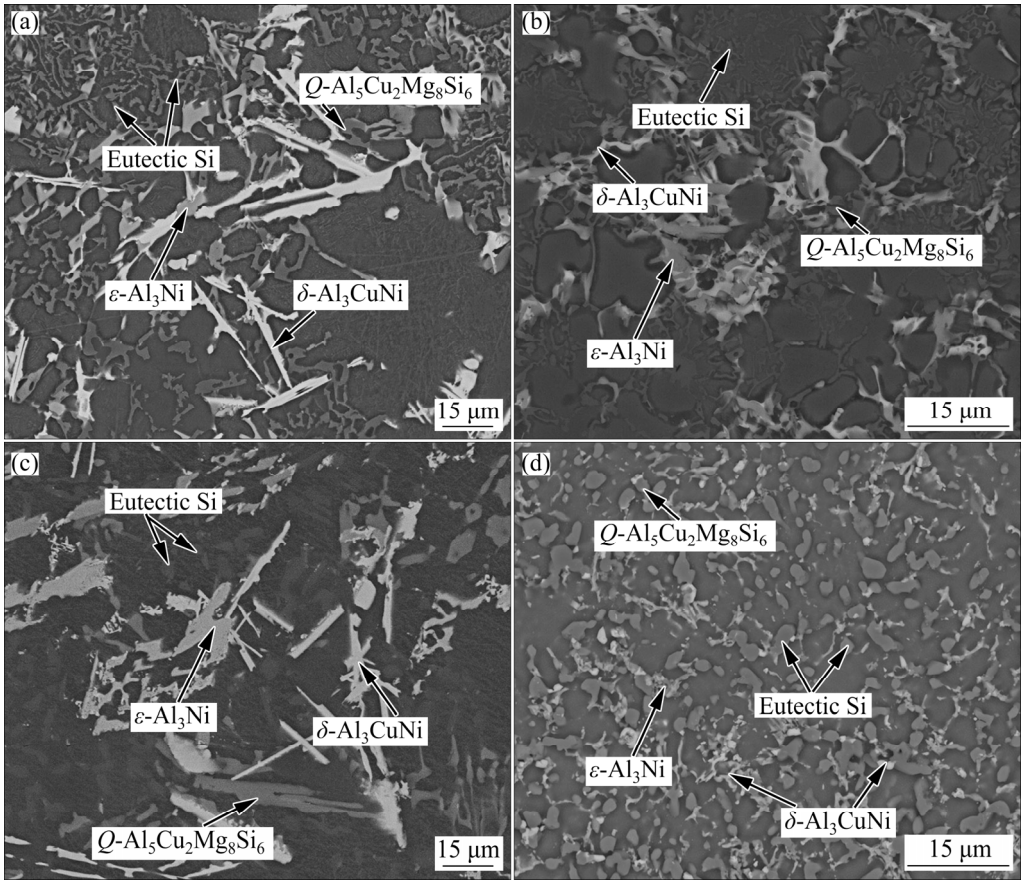

Fig. 3 Backscattered electron SEM images of intermetallics present in alloys: (a) PMC; (b) HPDC; (c) TEPMC; (d) TEHPDC

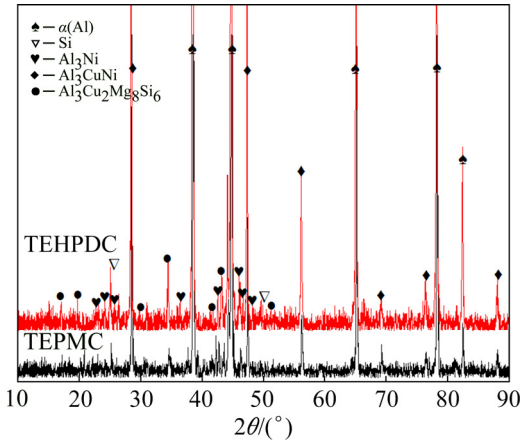

Fig. 4 XRD patterns of TEPMC and TEHPDC alloys

Figure 5 shows the morphology of eutectic Si in the two alloys before and after thermal exposure at 350 °C for 200 h. As displayed in Figs. 5(a) and (b), the Si particles exhibit an elongated rod-like morphology with sharp edges in both PMC and HPDC alloys. The Si particles become larger and more spherical without sharp edges for both alloys after thermal exposure, indicating that the eutectic Si is unstable at 350 °C. The aspect ratio, roundness, and size of eutectic Si are further characterized in detail as follows.

The effect of thermal exposure at 350 °C on the evolution of eutectic Si is quantitatively characterized. The distribution of the aspect ratio of eutectic Si for the studied alloys is shown in Fig. 6. After thermal exposure, the frequency with lower aspect ratio of eutectic Si particles increases at the cost of higher aspect ratio, and the average value decreases accordingly. For PMC, the average value of aspect ratio of eutectic Si decreases from 2.49 for PMC to 2.19 for TEPMC alloy. Also, for the HPDC and TEHPDC alloys, the average values are 2.9 and 1.85, respectively. After thermal exposure, around 70% eutectic Si particle in the TEHPDC sample exhibits an aspect ratio <2. This indicates that the shape of eutectic Si is gradually transformed from long-strip into sphere during thermal exposure at 350 °C.

Figure 7 shows the roundness distribution of the eutectic Si for the studied alloys. As shown in Fig. 7(a), the roundness of eutectic Si particles in

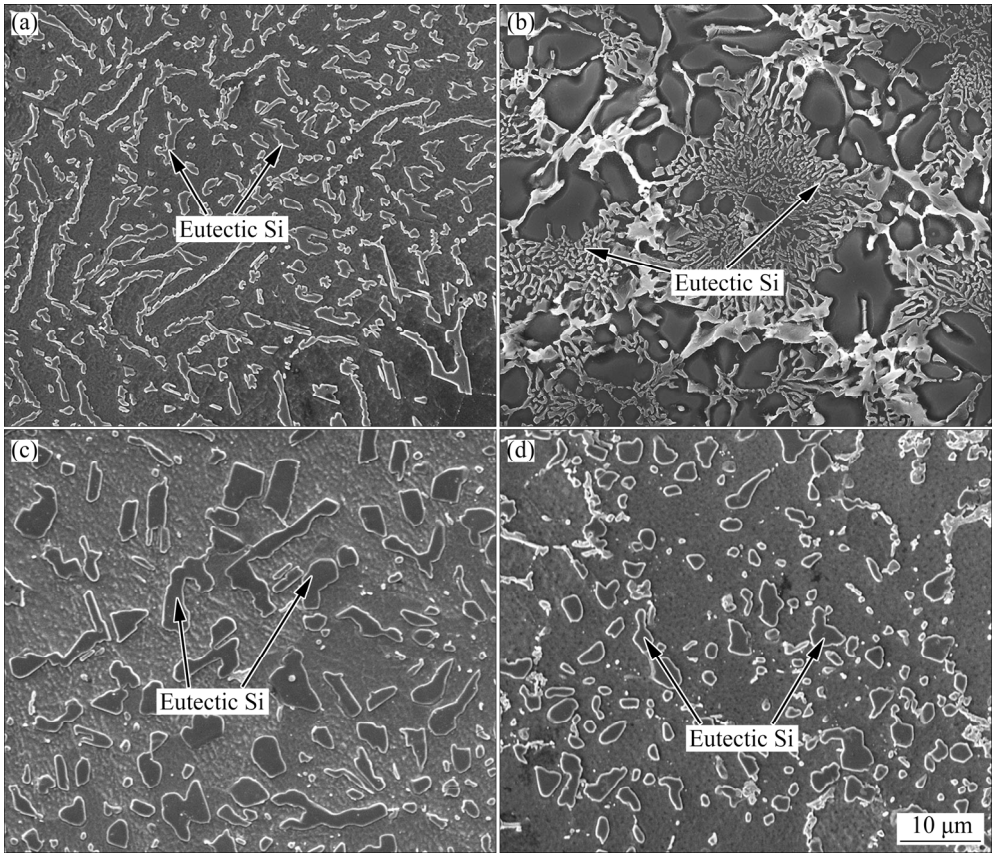

Fig. 5 Secondary electron SEM images of eutectic Si particles in studied alloys: (a) PMC; (b) HPDC; (c) TEPMC; (d) TEHPDC

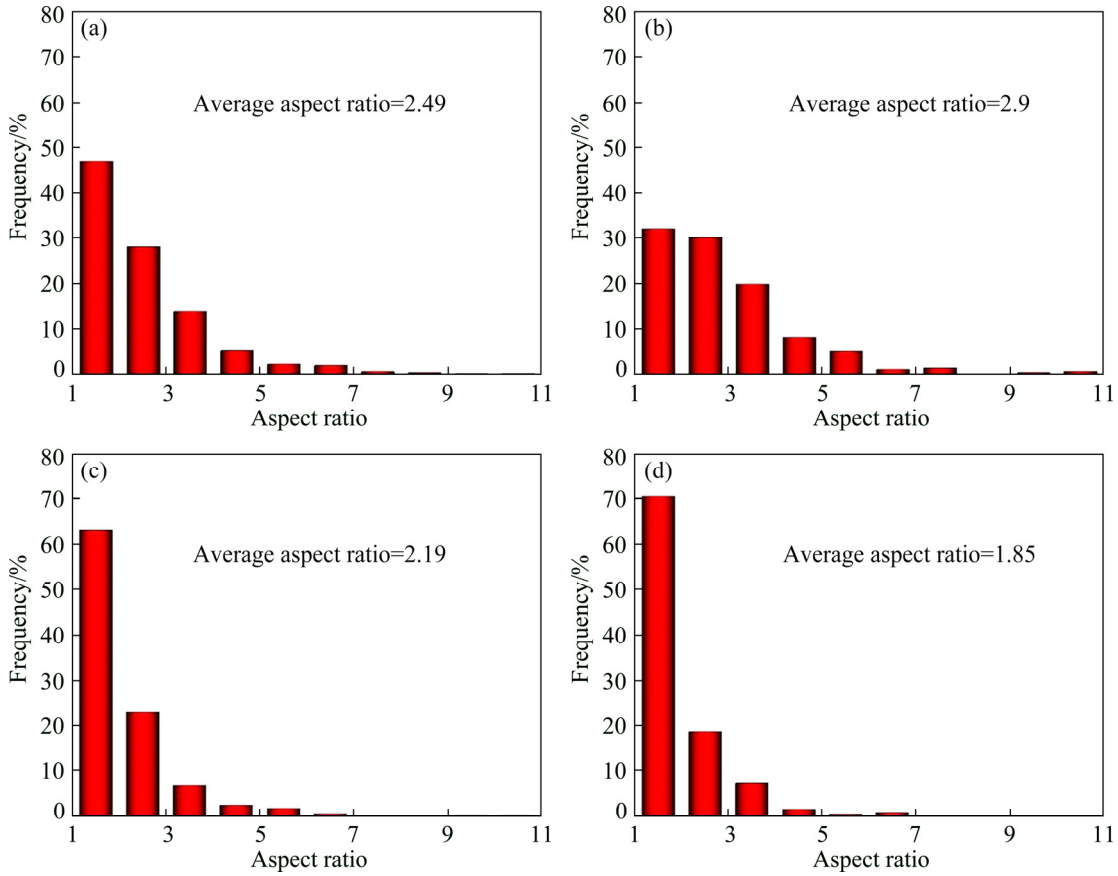

Fig. 6 Aspect ratio distribution of eutectic Si in studied alloys: (a) PMC; (b) HPDC; (c) TEPMC; (d) TEHPDC

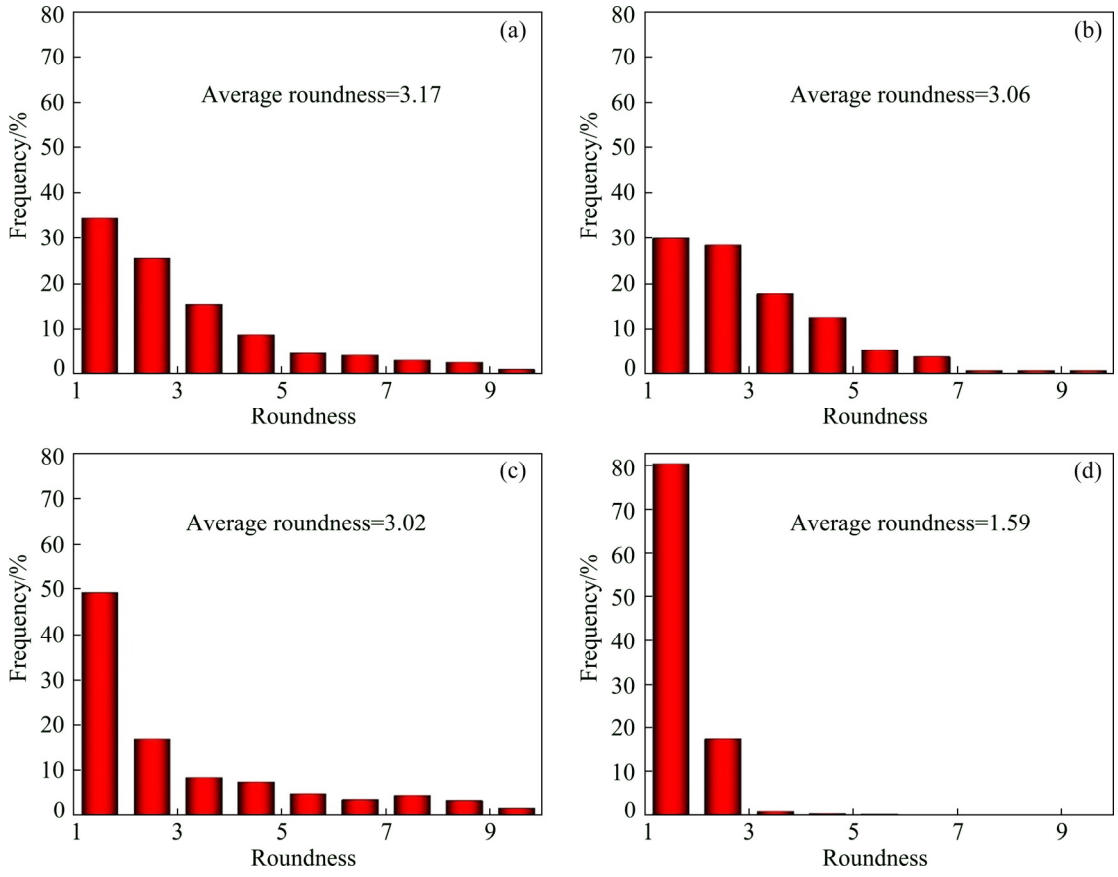

Fig. 7 Roundness distribution of eutectic Si in studied alloys: (a) PMC; (b) HPDC; (c) TEPMC; (d) TEHPDC

the PMC alloy is in the range of 1−10, and about 34% of them vary from 1 to 2. After thermal exposure, the number of the eutectic Si particles with a roundness lying in the range of 1−2 increases, as shown in Fig. 7(c), and the average value of the roundness decreases from 3.17 to 3.02. For the HPDC alloy, it is observed that the roundness of the eutectic Si particles dramatically decreases after thermal exposure. As shown in Fig. 7(b), the roundness of the eutectic Si particles in the HPDC alloy is in the range of 1−10, and only 30% of them are in the range of 1−2. For the TEHPDC alloy, nearly 81% of eutectic Si particles have small roundness (<2), and the average roundness is greatly reduced from 3.06 to 1.59. The reduction of eutectic Si roundness during thermal exposure is attributed to spheroidizing, which is driven by reducing the surface energy and elastic strain energy [24]. Therefore, the reduction of eutectic Si roundness of the HPDC alloy with smaller particle size and higher surface energy is much more significant than that of the PMC alloy.

Figure 8 shows the size distribution of eutectic Si particles in the studied alloys. The data on size distribution were analyzed by curve fitting using the maximum likelihood estimation (MLE) method [25]. The results show that the eutectic Si sizes of the PMC and TEPMC alloys follow the log-normal distribution. The average sizes of eutectic Si particles for PMC and TEPMC alloys are 1.4 and 1.8 μm, respectively. By contrast, the initial normal distribution of eutectic Si particles for the HPDC alloy transforms into the log-normal distribution for the TEHPDC alloy. The average sizes of eutectic Si particles of the HPDC and TEHPDC alloys are 0.4 and 1.6 μm, respectively. The coarsening of eutectic Si particles may follow the Ostwald ripening mechanism where larger particles grow at the expense of the smaller ones. Meanwhile, adjacent eutectic Si particles tend to overlap and aggregate when the atomic matching between the contacted surfaces of two particles is beneficial for crystal growth. These coarsening processes are favorable from the thermodynamic point of view where the system tends to lower interfacial energy reported in many studies [26−28].

An interesting phenomenon is that both TEHPDC and TEPMC alloys exhibit almost equal mean size of eutectic Si particles, which reveals that

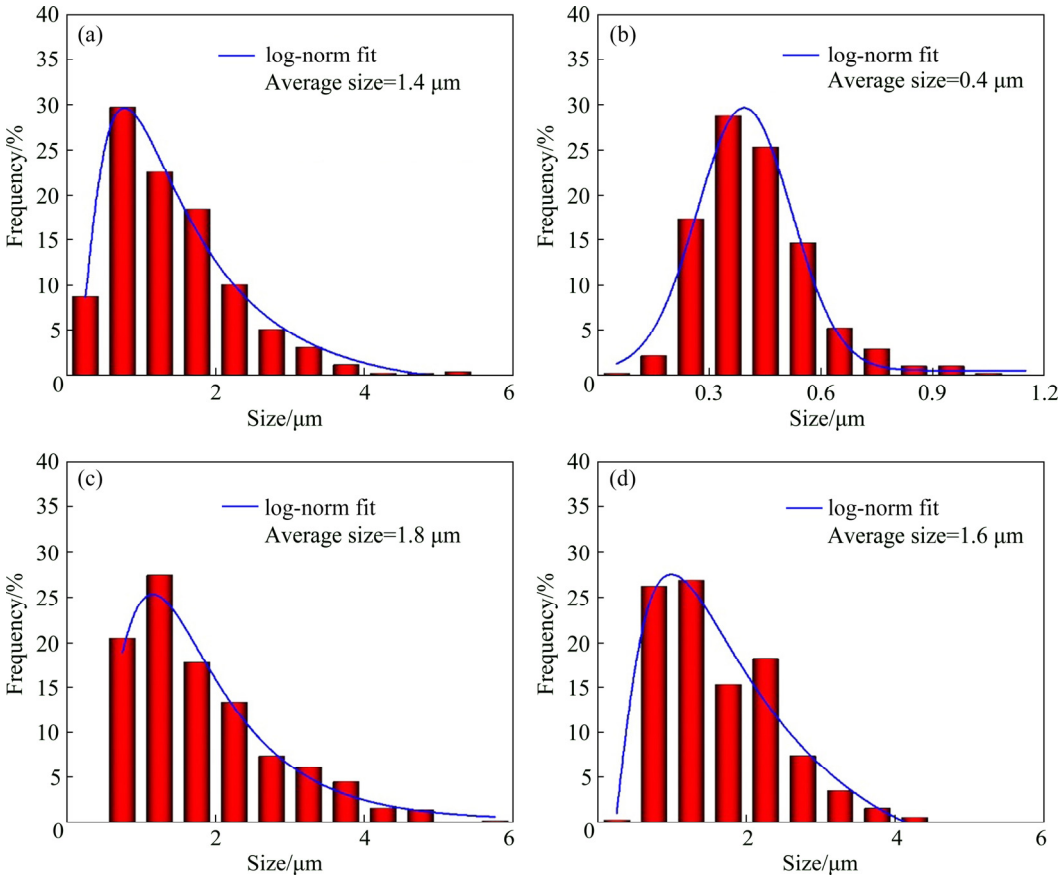

Fig. 8 Size distribution of eutectic Si in studied alloys: (a) PMC; (b) HPDC; (c) TEPMC; (d) TEHPDC

the coarsening rate of eutectic Si is higher for the smaller mean size in the high pressure die casting alloy. As described in Ref. [29], the solidification rate of HPDC is about 10 times higher than that of PMC, leading to finer microstructure for HPDC alloy. Possibly due to high pressure during rapid solidification for the HPDC alloy, elastic energy is stored and less energy is required to activate the diffusion process during thermal exposure. Furthermore, smaller size results in higher surface energy and shorter inter-particle spacing between eutectic Si particles, and it is favorable for inter-particle diffusion and coarsening for the HPDC alloy.

3.2 Tensile properties

The yield strength (YS), ultimate tensile strength (UTS), and elongation (δ) of the studied alloys at both room temperature and 350 °C are summarized in Table 1. After thermal exposure at 350 °C for 200 h, the UTS of the PMC alloy decreases from 244 to 208 MPa at room temperature. However, the elongation increases from 0.69% to 1.1%. In the case of HPDC processing, the UTS declines from 310 MPa for HPDC alloy to 246 MPa for TEHPDC alloy, while the elongation increases from 0.35% to 1.3% for TEHPDC alloy. The reduction of tensile strength for the alloys after thermal exposure is attributed to the coarsening of Si phase, which means that the load bearing capacity of the alloys is decreased after thermal exposure. The spheroidization of the Si particles is believed to be the main mechanism for the high elongation. According to the Hall−Patch relationship, the TEHPDC alloy shows superior tensile properties compared to the TEPMC alloy at room temperature possibly related to the microstructure refinement and homogenization for the TEHPDC alloy. The small grain size existing in the TEHPDC alloy is due to the rapid cooling rate during the die casting process.

As shown in Table 1, the tensile strength of the alloys decreases after thermal exposure at elevated temperature and the elongation of the alloys shows a reverse trend. It should be noted that the tensile strength of the HPDC alloy is much higher than that of the PMC alloy at elevated temperature before thermal exposure. However, the tensile strength of the TEHPDC alloy is nearly the same as the TEPMC alloy. In general, grain boundary strengthening is not apparent for enhancing high temperature strength due to the occurrence of cross-slips induced by thermally activated process. Thermally stable phases such as δ-Al_3CuNi remain almost unchanged during thermal exposure shown in Fig. 3, which means that these stable phases do not lead to the tensile strength decreasing tested at 350 °C. Combining the statistical average particle size of the eutectic Si shown in Fig. 8, it is found that the alloys with smaller size have higher tensile strength at 350 °C as shown in Table 1. The TEHPDC and TEPMC alloys exhibit a similar eutectic Si size and similar tensile strength at elevated temperature. Consequently, it is reasonable to infer that for Al−Si eutectic alloys the tensile properties at high temperature have close relations with the size and distribution of Si phase. These phenomena observed for TEPMC and TEHPDC alloys are in good agreement with dispersion hardening model [30,31]. Therefore, to stablize the eutectic Si phase may be an effective way to enhance the tensile strength at evelated temperatures.

Figure 9 shows the fracture surfaces of the TEPMC and TEHPDC alloys tested at room temperature. For the TEPMC alloy, mixed-rupture characteristics are observed as dimples in α(Al) and cleavage cracks and cleavage facets in brittle phases (Figs. 9(a) and (b)). Some dimples are found in the Al matrix, indicating the plastic deformation of the

Table 1 Tensile properties of studied alloys at room temperature and 350 °C

Alloy	At room temperature			At 350 °C		
	UTS/MPa	YS/MPa	δ/%	UTS/MPa	YS/MPa	δ/%
PMC [18]	244	221	0.69	101	81	4.3
HPDC [18]	310	282	0.35	135	103	5.6
TEPMC	208	204	1.1	68	67	5.8
TEHPDC	246	213	1.3	67	66	6.7

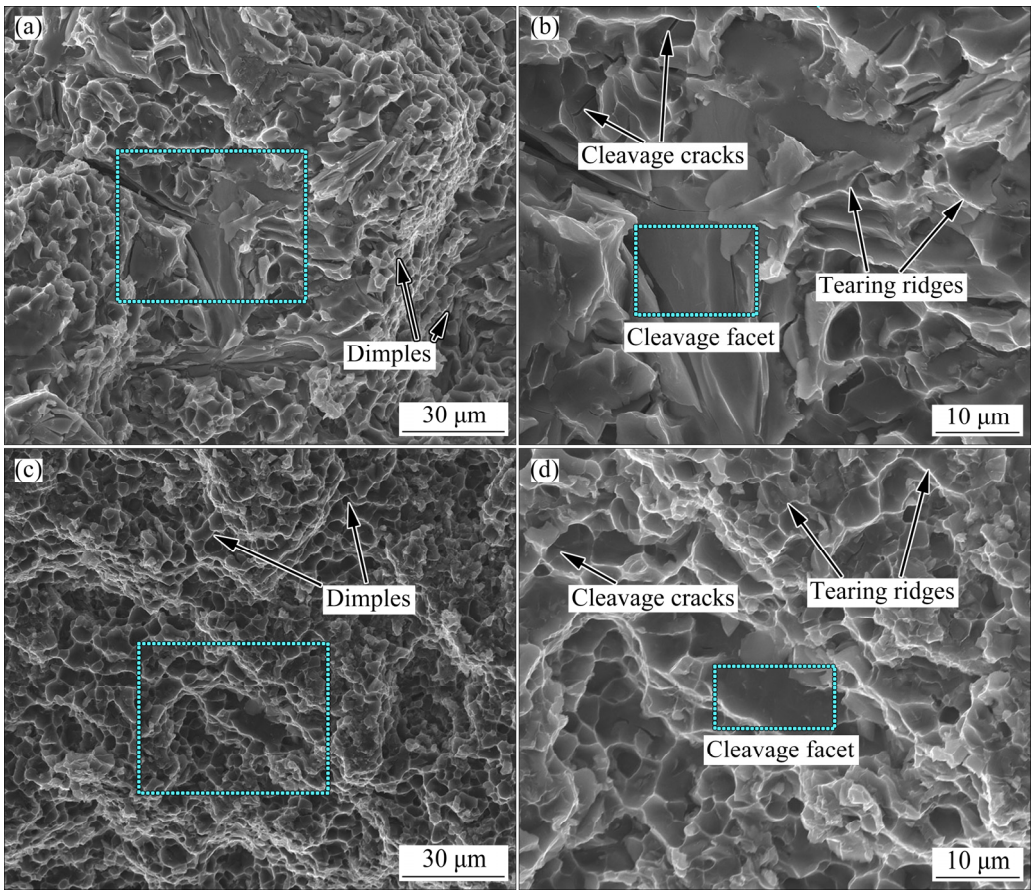

Fig. 9 Fractographs of TEPMC (a, b) and TEHPDC (c, d) alloys tested at room temperature after thermal exposure

ductile matrix. During tensile testing, the plastic deformation of the Al matrix leads to dislocation pileup along the interface of the brittle intermetallic phase and Al matrix, resulting in crack initiation on the hard phase due to the stress concentration [32]. Similar fracture characteristic is also observed for the TEHPDC alloy, although dimples and brittle facets are much finer and more uniform, which is consistent with higher elongation of the TEHPDC alloys after thermal exposure. Previous work found that the PMC and HPDC alloys before thermal exposure exhibited brittle fracture at room temperature [18]. The transition from a brittle fracture mode to a mixed-rupture mode is identified after thermal exposure, which is consistent with the increase of the elongation.

The fracture surfaces of the TEPMC and TEHPDC alloys tested at 350 °C are illustrated in Fig. 10. For the TEPMC and TEHPDC alloys, the fracture surfaces exhibit large amounts of micro-voids and deep dimples marked with blue arrows, which are the characteristics of ductile fracture. At the same time, slip lines enclosed by the blue boxes (Figs. 10(b) and (d)) are found, suggesting that the plastic deformation occurs in the α(Al) matrix. During tensile process at the elevated temperature, micro-voids nucleate in the soft matrix due to the localized strain discontinuity along the interface between soft matrix and brittle phases and blunt cracking. Subsequently, the micro-voids grow, coalesce and ultimately lead to the rupture of the specimens with the continuous increase of external load. In addition, the size of dimples for TEHPDC alloy is smaller than that of TEPMC alloy, and the depth of the dimples of TEHPDC alloy is higher than that of TEPMC alloy, which is consistent with the higher elongation of TEHPDC alloy.

3.3 Compression creep behavior

Figure 11 shows the typical compression creep curves of the alloys tested at 250 °C and under stress levels ranging from 20 to 130 MPa. Creep strain increases with the applied external stress, and significant plastic deformation occurs with accumulated creep strain above 15% when the external stress reaches 100 MPa for both TEPMC

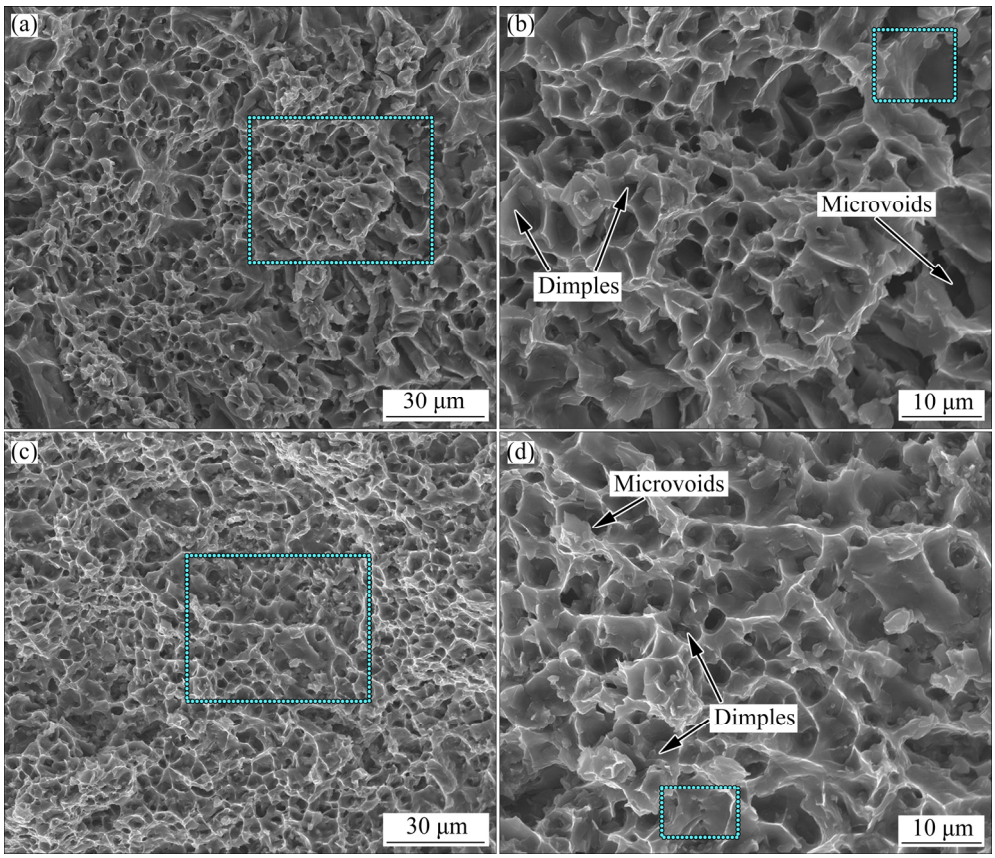

Fig. 10 Fractographs of alloys tested at 350 °C after thermal exposure: (a, b) TEPMC; (c, d) TEHPDC

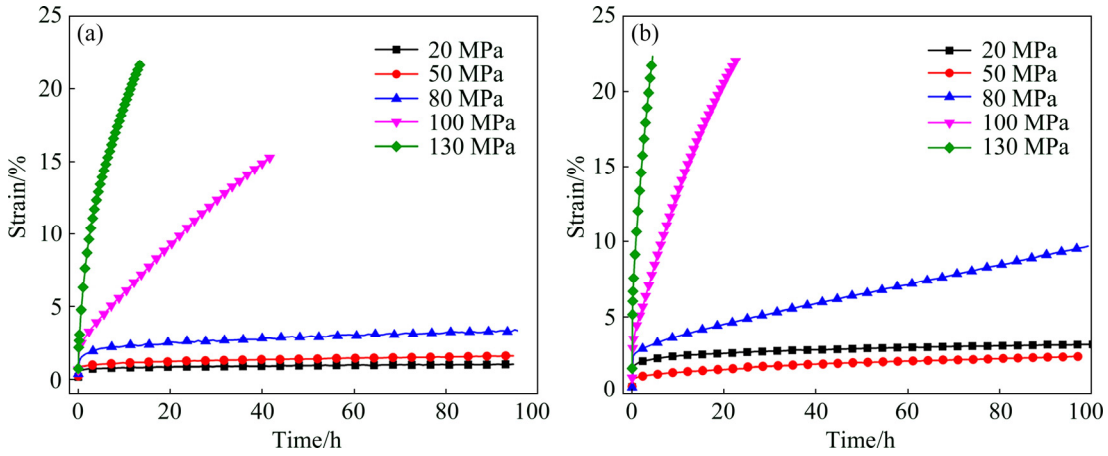

Fig. 11 Typical compressive creep curves of alloys tested at 250 °C and under stresses ranging from 20 to 130 MPa: (a) TEPMC; (b) TEHPDC

and TEHPDC alloys holding for 100 h at 250 °C. In contrast, the creep strain gets stabilized when the applied creep stress is less than 50 MPa, and the total creep strain is less than 2%.

The creep strain rate is calculated by differentiating strain with respect to time, and the curves consist of the primary creep stage and secondary creep stage based on creep strain rate. At the primary creep stage, the creep strain rate decreases with increasing creep time due to working hardening. In the secondary creep stage, the creep strain rate reaches the minimum value and becomes constant, and the constant creep rate is called steady-state creep rate. The steady creep stage is dominant during the compression creep. The minimum creep rates of the investigated alloys

under various creep conditions are shown in Fig. 12. The minimum creep rates of the alloys after thermal exposure are higher than those of the as-cast alloys, indicating that the reduction in creep resistance occurs after thermal exposure. In addition, the minimum creep rates of the TEHPDC alloy are higher than those of the TEPMC alloy under various creep conditions, which means that the TEPMC alloy has better creep resistance than the TEHPDC alloy. However, a reverse trend in the high-stress and high temperature regions is observed for HPDC and PMC alloys before thermal exposure.

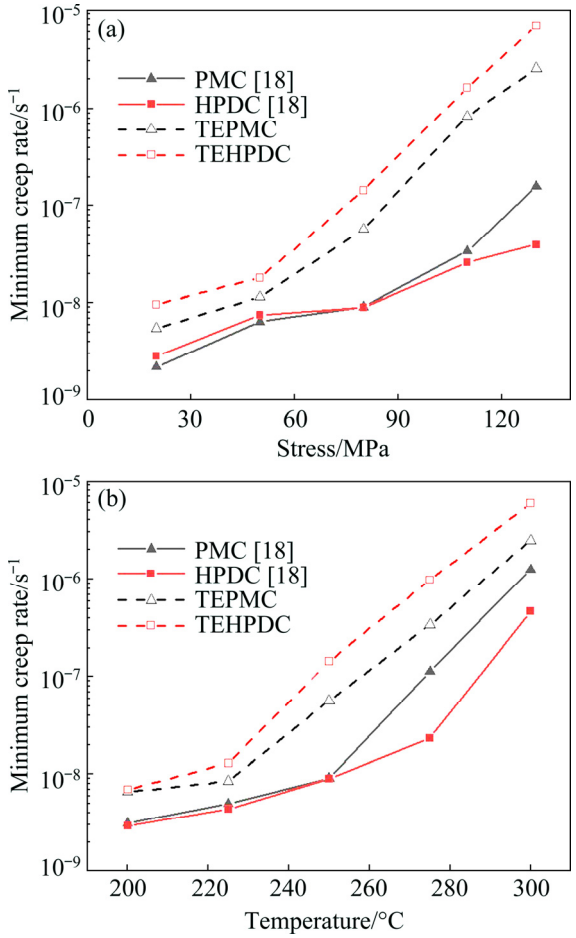

Fig. 12 Minimum creep rates of investigated alloys treated at 250 °C and stresses of 20−130 MPa (a), and at temperatures of 200−300 °C under stress of 80 MPa (b)

The minimum creep rate has strong relation with creep temperature and applied stress, which is generally characterized by the following power-law type constitutive equation [18]:

$$\dot{\varepsilon} = A_0\sigma^n \exp(-\frac{Q}{RT}) \quad (2)$$

where $\dot{\varepsilon}$ is the minimum creep rate, A_0 is the material constant, σ is the applied creep stress, n is the stress exponent, Q is the activation energy, R is the universal gas constant, and T is the thermodynamic temperature. Figure 13(a) shows the log plots of the minimum creep rate versus applied stress based on Eq. (2) for the TEPMC and TEHPDC alloys at 250 °C. There is a clear transition at 50 MPa, and the creep stress can be divided as low stress region (≤50 MPa) and high stress region (>50 MPa). The n values in the low stress region for the TEPMC and TEHPDC alloys are 0.69 and 0.81, respectively, while the n values in the high stress region are 6.18 and 5.75, respectively. Figure 13(b) shows the Arrhenius plot of the minimum creep rate versus $T^{-1}/10^{-3}R$ on log-linear axes for the TEPMC and TEHPDC alloys at 80 MPa. The activation energy (Q) also exhibits two different regions at the transition point of 225 °C. In the low temperature region, the Q values of the TEPMC and TEHPDC alloys are 20.0 and 48.9 kJ/mol, respectively. The Q values are higher

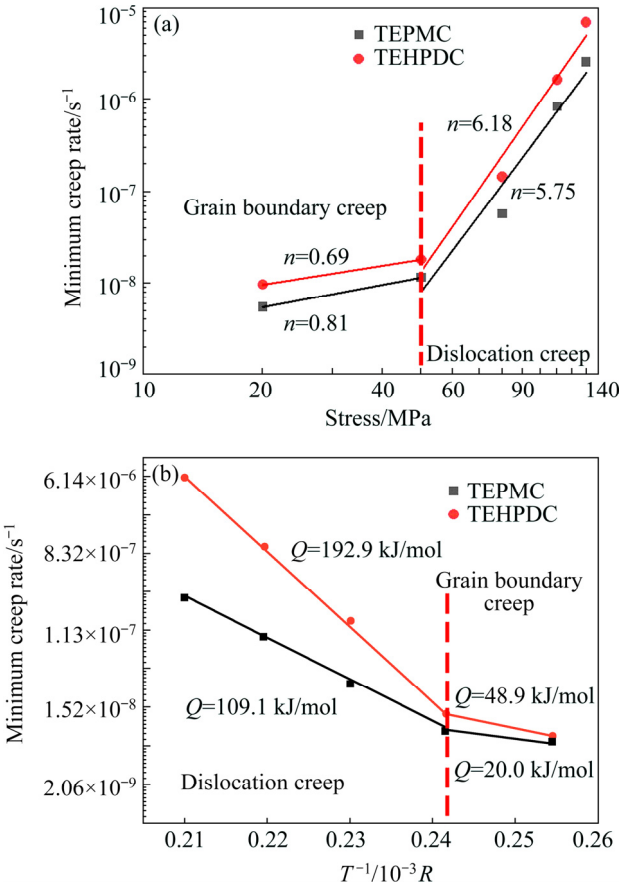

Fig. 13 Creep mechanism of TEPMC and TEHPDC alloys based on power-law: (a) Stress exponent; (b) Activation energy

in the high temperature (>225 °C) region, that is, 109.1 and 192.9 kJ/mol for the TEPMC and TEHPDC alloys, respectively.

The determination of stress exponent and activation energy is an available guide to evaluate different dominant creep mechanisms. It is generally accepted that diffusion creep (n=1), grain boundary sliding (n=2) and dislocation creep (n=3−7) are three main creep mechanisms for aluminum alloys [33,34]. The corresponding activation energy gives the information about the specific diffusion mode under a certain creep mechanism. As reported by FROST and ASHBY [35], the typical activation energies for grain boundary diffusion and lattice self-diffusion in pure Al are 82 and 142 kJ/mol, respectively. The stress exponents of the TEPMC and TEHPDC alloys are lower than 2, indicating that the grain boundary creep dominates the secondary creep stage in the low stress region. Dislocation climb is considered to make strong contribution to the secondary-stage creep, especially when the n values are 4−7 in the high stress region for both alloys. The different creep activation energies also indicate a variation of the creep mechanism in the different temperature regions. The Q values (20 and 48.9 kJ/mol) of the TEPMC and TEHPDC alloys in the low temperature region indicate that grain boundary creep is regarded as the predominant steady-state creep mechanism. In the high temperature region, the Q values are consistent with the dislocation creep for the aluminum alloys.

When the applied stress level is below 50 MPa and service temperature is below 225 °C, grain boundary creep mechanism dominates with low stress component <1 and low activation energy. Similar trend was found in both alloys before thermal exposure. Grain boundary creep is the dominant mechanism in the low stress and temperature regions, while dislocation climb is suggested to control the creep in the high stress and temperature regions [18]. However, after thermal exposure the critical stress and critical temperature for distinguishing different creep deformation mechanisms diminish from 80 to 50 MPa and from 250 to 225 °C, respectively. The decrease of creep resistance resulting in creep mechanism transition is consistent with the study by PANDEY et al [34].

4 Conclusions

(1) The spheroidization and coarsening of eutectic Si occur during the thermal exposure at 350 °C. Although the HPDC alloy has much smaller size of eutectic Si than PMC alloy, the sizes of eutectic Si particles of the TEHPDC and TEPMC alloys after thermal exposure are almost equal.

(2) Thermal exposure results in a decrease in tensile strength and an increase in ductility of thermally exposed alloys compared with the corresponding as-cast alloys. The tensile strength of the TEHPDC alloy at room temperature is higher than that of the TEPMC alloy. However, the tensile strength of the TEHPDC alloy at 350 °C is almost identical to that of the TEPMC alloy, which is mainly ascribed to the equal size of eutectic Si obtained in the TEPMC and TEHPDC alloys.

(3) The minimum creep rates of both alloys after thermal exposure are higher than those of the as-cast alloys. The TEPMC alloy exhibits better creep resistance than the TEHPDC alloy in the high stress and high temperature regions controlled by dislocation creep mechanism, while a reverse trend of creep resistance is observed for HPDC and PMC alloys before thermal exposure.

(4) Al−Si eutectic alloys with a small size of eutectic Si particles produced by HPDC technology are not suitably used at 350 °C due to the rapid coarsening of eutectic Si.

References

[1] PUNCREOBUTR C, LEE P D, KAEH K M, CONNOLLEY T, FIFE J L, PHILLION A B. Influence of Fe-rich intermetallics on solidification defects in Al−Si−Cu alloys [J]. Acta Materialia, 2014, 68(15): 42−51.

[2] HU Ze-yi, FAN Cai-he, ZHENG Dong-sheng, LIU Wen-liang, CHEN Xi-hong. Microstructure evolution of Al−Cu−Mg alloy during rapid cold punching and recrystallization annealing [J]. Transactions of Nonferrous Metals Society of China, 2019, 29: 1816−1823.

[3] ALEMDAG Y, BEDER M. Effects of zinc content on strength and wear performance of Al−12Si−3Cu based alloy [J]. Transactions of Nonferrous Metals Society of China, 2019, 29: 2463−2471.

[4] CAI Zhi-yong, ZHANG Chun, WANG Ri-chu, PENG Chao-qun, WU Xiang, LI Han-pu, YANG Ming. Improvement of deformation capacity of gas-atomized hypereutectic Al−Si alloy powder by annealing treatment [J]. Transactions of Nonferrous Metals Society of China, 2018, 28: 1475−1483.

[5] XU Rui, LIN Bo, LI Hao-yu, XIAO Hua-qiang, ZHAO Yu-liang, ZHANG Wei-wen. Microstructure evolution and mechanical properties of Al−6.5Cu−0.6Mn−0.5Fe alloys with different Si additions [J]. Transactions of Nonferrous Metals Society of China, 2019, 29: 1583−1591.

[6] HEKIMOGLU A P, CALIS M. Effects of titanium addition on structural, mechanical, tribological, and corrosion properties of Al−25Zn−3Cu and Al−25Zn−3Cu−3Si alloys [J]. Transactions of Nonferrous Metals Society of China, 2020, 30: 303−317.

[7] ZOU Li-jie, YE Bing, FENG Jian, XU Xiao-jing, KONG Xiang-yang, JIANG Hai-yan. Effect of δ-Al_3CuNi phase and thermal exposure on microstructure and mechanical properties of Al−Si−Cu−Ni alloys [J]. Journal of Alloys and Compounds, 2019, 791: 1015−1024.

[8] FENG Jian, YE Bing, ZUO Ll-jie, QI Rui-juan, WANG Qu-dong, JIANG Hai-yan, HUANG Rong, DING Wen-jiang. Effects of Ni content on low cycle fatigue and mechanical properties of Al−12Si−0.9Cu−0.8Mg−xNi at 350 °C [J]. Materials Science and Engineering A, 2017, 706: 27−37.

[9] SHAHA S K, CZERWINSKI F, KASPRZAK W, FRIEDMAN J, CHEN D L. Effect of Mn and heat treatment on improvements in static strength and low-cycle fatigue life of an Al−Si−Cu−Mg alloy [J]. Materials Science and Engineering A, 2016, 657: 441−452.

[10] ZUO Li-jie, YE Bing, FENG Jian, KONG Xiang-yang, JIANG Hai-yan, DING Wen-jiang. Effect of Q-$Al_5Cu_2Mg_8Si_6$ phase on mechanical properties of Al−Si−Cu−Mg alloy at elevated temperature [J]. Materials Science and Engineering A, 2017, 693: 26−32.

[11] LI Guang-jin, LIAO Heng-cheng SUO Xiao-jing, TANG Yun-yi, DIXIT U S, PETROV P. Cr-induced morphology change of primary Mn-rich phase in Al−Si−Cu−Mn heat resistant aluminum alloys and its contribution to high temperature strength [J] Materials Science and Engineering A, 2018, 709: 90−96.

[12] ANAS N S, RAMAKRISHNA M, DASH R K, RAO T N, VIJAY R. Influence of process control agents on microstructure and mechanical properties of Al alloy produced by mechanical alloying [J]. Materials Science and Engineering A, 2019, 751: 171−182.

[13] PARK J M, KIM K B, KIM D H, MATTERN N, LI R, LIU G, ECKERT J. Multi-phase Al-based ultrafine composite with multi-scale microstructure [J]. Intermetallics, 2010, 18(10): 1829−1833.

[14] DU Xiao-fan, GAO Tong, LIU Gui-liang, LIU Xiang-fa. In situ synthesizing SiC particles and its strengthening effect on an Al−Si−Cu−Ni−Mg piston alloy [J]. Journal of Alloys and Compounds, 2017, 695: 1−8.

[15] HAN Li-na, SUI Yu-dong, WANG Qu-dong, WANG Kui, JIANG Ye-hua. Effects of Nd on microstructure and mechanical properties of cast Al−Si−Cu−Ni−Mg piston alloys [J]. Journal of Alloys and Compounds, 2017, 695: 1566−1572.

[16] PRAMOD S L, RAVIKIRANA A K, RAO P, MURTY B S, BAKSHI S R. Microstructure and mechanical properties of as-cast and T6 treated Sc modified A356-5TiB2 in-situ composite [J]. Materials Science and Engineering A, 2019, 739: 383−394.

[17] ZHANG X, HUANG L K, ZHANG B, CHEN Y Z, DUAN S Y, LIU G, YANG C L, LIU F. Enhanced strength and ductility of A356 alloy due to composite effect of near-rapid solidification and thermo-mechanical treatment [J]. Materials Science and Engineering A, 2019, 753: 168−178.

[18] ZUO Li-jie, YE Bing, FENG Jian, KONG Xiang-yang, JIANG Hai-yan, DING Wen-jiang. Microstructure, tensile properties and creep behavior of Al−12Si−3.5Cu−2Ni−0.8Mg alloy produced by different casting technologies [J]. Journal of Materials Science and Technology, 2018, 34(7): 1222−1228.

[19] BUGELNIG K, SKET F, GERMANN H, STEFFENS T, KOOS R, WILDE F, BOLLER E, REQUENA G. Influence of 3D connectivity of rigid phases on damage evolution during tensile deformation of an AlSi12Cu4Ni2 piston alloy [J]. Materials Science and Engineering A, 2018, 709: 193−202.

[20] DEZECOT S, MAUREL V, BUFFIERE J Y, SZMYTKA F, KOSTER A. 3D characterization and modeling of low cycle fatigue damage mechanisms at high temperature in a cast aluminum alloy [J]. Acta Materialia, 2017, 123: 24−34.

[21] ASGHAR Z, REQUENA G, BOLLER E. Three-dimensional rigid multiphase networks providing high-temperature strength to cast AlSi10Cu5Ni1-2 piston alloys [J]. Acta Materialia, 2011, 59(16): 6420−6432.

[22] ASGHAR Z, REQUENA G, DEGISCHER H P, CLOETENS P. Three-dimensional study of Ni aluminides in an AlSi12 alloy by means of light optical and synchrotron microtomography [J]. Acta Materialia, 2009, 57(14): 4125−4132.

[23] ZOU Li-jie, YE Bing, FENG Jian, ZHANG Hui-xia, XU Xiao-jiang, KONG Xiang-yang, JIANG Hai-yan. Effect of ε-Al_3Ni phase on mechanical properties of Al–Si–Cu–Mg–Ni alloys at elevated temperature [J]. Materials Science and Engineering A, 2020, https://doi.org/10.1016/j.msea.

[24] LIN Y C, LUO Shun-cun, HUANG Jian, YIN Liang-xing, JIANG Xing-you. Effects of solution treatment on microstructures and micro-hardness of a Sr-modified Al−Si−Mg alloy [J]. Materials Science and Engineering A, 2018, 725: 530−540.

[25] EISAABADI G B, YEOM G Y, TIRYAKIOGLU M, NETTO N, BEYGI R, MEHRIZI M Z, KIM S K. The effect of solution treatment time on the microstructure and ductility of naturally-aged A383 alloy die castings [J]. Materials Science and Engineering A, 2018, 722: 1−7.

[26] HE Tian-bing, ERTUGRUL O, CIFTCI N, UHLENWINKEL V, NIELSCH K, SCUDINO S. Effect of particle size ratio on microstructure and mechanical properties of aluminum matrix composites reinforced with Zr48Cu36Ag8Al8 metallic glass particles [J]. Materials Science and Engineering A, 2019, 742: 517−525.

[27] LUMLEY R N, ODONNELL R G, GUNASEGARAM D R, GIVORD M. Heat treatment of high-pressure die castings [J]. Metallurgical and Materials Transactions A, 2007, 38(10): 2564−2574.

[28] RATKE L, VOORHEES P W. Growth and coarsening: Ostwald ripening in material processing [M]. New York: Springer, 2002.

[29] BAI Jing, SUN Yang-shan, XUE Feng, QIANG Jing.

Microstructures and creep properties of Mg−4Al−(1−4)La alloys produced by different casting techniques [J]. Materials Science and Engineering A, 2012, 552: 472−480.

[30] ASGHAR Z, REQUENA G. Three dimensional post-mortem study of damage after compression of cast Al−Si alloys [J]. Materials Science and Engineering A, 2014, 591: 136−143.

[31] CACERES C H, GRIFFITHS J R, REINER P. The influence of microstructure on the Bauschinger effect in an AlSiMg casting alloy [J]. Acta Materialia, 1996, 44(1): 15−23.

[32] YIN De-yan, XIAO Qiao, CHEN Yu-qiang, LIU Hui-qun, YI Dang-qing, WANG Bin, PAN Su-ping. Effect of natural ageing and pre-straining on the hardening behaviour and microstructural response during artificial ageing of an Al−Mg−Si−Cu alloy [J]. Materials Design, 2016, 95: 329−339.

[33] LI Y, LANGDON T G. Creep behavior of a reinforced Al-7005 alloy: Implications for the creep processes in metal matrix composites [J]. Acta Materialia, 1998, 46(4): 1143−1155.

[34] PANDEY A B, MISHRA R S, PARADKAR A G, MAHAJAN Y R. Steady state creep behaviour of an Al−Al_2O_3 alloy [J]. Acta Materialia, 1997, 45(3): 1297−1306.

[35] FROST H J, ASHBY M F. Deformation-mechanism maps: The plasticity and creep of metals and ceramics [M]. Pergamon: Pergamon Press, 1982.

热暴露对不同铸造工艺 Al−Si−Cu−Ni−Mg 合金组织和性能的影响

张嘉盈[1]，左立杰[2]，冯 剑[3]，叶 兵[1]，孔向阳[4]，蒋海燕[1]，丁文江[1]

1. 上海交通大学 轻合金精密成型国家工程研究中心与金属基复合材料国家重点实验室，上海 200240；
2. 江苏海洋大学 机械与海洋工程学院，连云港 222005；
3. 有研工程技术研究院有限公司，北京 101407；
4. 上海交通大学 材料科学与工程学院 移动能源材料研究所，上海 200240

摘 要：研究 350 °C 热暴露 200 h 对金属型铸造与高压铸造 Al−Si−Cu−Ni−Mg 合金组织和力学性能的影响。用扫描电镜和图片分析软件 IPP 表征合金中硅相的形貌。研究结果表明，高温热暴露促进共晶硅的球化和粗化。热暴露后，高压铸造合金的室温抗拉强度高于金属型铸造的，但 350 °C 时两种合金的高温抗拉强度均为 67 MPa 左右。由于共晶硅的粗化，热暴露后金属型铸造合金的抗蠕变性能均优于高压铸造合金。因此，拥有细小尺寸共晶硅的合金不适于在 350 °C 的条件下应用。

关键词：Al−Si−Cu−Ni−Mg 合金；热暴露；粗化；蠕变行为

(Edited by Xiang-qun LI)